Multinucleon transfer study in ^{206}Pb(^{18}O, x) at energies above the Coulomb barrier

Sonika, B. J. Roy,[*] A. Parmar, U. K. Pal, H. Kumawat, V. Jha, S. K. Pandit, V. V. Parkar, K. Ramachandran, K. Mahata,
A. Pal, S. Santra, and A. K. Mohanty

Nuclear Physics Division, Bhabha Atomic Research Centre, Mumbai 400 085, India

K. Sekizawa[†]

Faculty of Physics, Warsaw University of Technology, ulica Koszykowa 75, 00-662 Warsaw, Poland
and Graduate School of Pure and Applied Sciences, University of Tsukuba, Tsukuba 305-8571, Japan

Single- and multi-nucleon transfer reactions, namely, ^{206}Pb(^{18}O, ^{20}O), ^{206}Pb(^{18}O, ^{19}O), ^{206}Pb(^{18}O, ^{17}O), ^{206}Pb(^{18}O, ^{16}O), ^{206}Pb(^{18}O, ^{18}N), ^{206}Pb(^{18}O, ^{17}N), ^{206}Pb(^{18}O, ^{16}N), ^{206}Pb(^{18}O, ^{15}N), ^{206}Pb(^{18}O, ^{14}N), ^{206}Pb(^{18}O, ^{16}C), ^{206}Pb(^{18}O, ^{15}C), ^{206}Pb(^{18}O, ^{14}C), ^{206}Pb(^{18}O, ^{13}C), ^{206}Pb(^{18}O, ^{12}C), ^{206}Pb(^{18}O, ^{12}B), ^{206}Pb(^{18}O, ^{11}B), ^{206}Pb(^{18}O, ^{10}B), ^{206}Pb(^{18}O, ^{10}Be), and ^{206}Pb(^{18}O, ^{9}Be), have been studied at an incident ^{18}O energy of 139 MeV. The total kinetic energy loss (TKEL) spectrum and angular distribution of reaction products have been measured. The Q value and angle integrated cross sections are deduced. Angular distributions for the elastically scattered ^{18}O particles are also measured. Fully microscopic time-dependent Hartree-Fock (TDHF) calculations, based on the independent single-nucleon transfer mode, have been carried out and are compared with experimental data of multinucleon transfer reactions. The TDHF calculations provide reasonable agreement with the experimental data for cases where one- and two-nucleon transfer is involved; the discrepancy is large for multinucleon transfer reactions. The effect of particle evaporation on the production cross sections has been studied. Inclusion of particle evaporation effects, though improving the results, could not reproduce the measured cross sections. Possible origins of these discrepancies are discussed.

I. INTRODUCTION

In reactions between two complex nuclei, a large number of nucleons transferred from projectile to target and vice versa have been often observed to occur with a probability comparable to that of single nucleon transfer, and they account for a significant fraction of the total reaction cross section. The multinucleon transfers between heavy ions play important role for definition of the reaction mechanism that describes evolution of the reaction from the quasielastic regime to more complex deep-inelastic reactions and provide detailed insight into the underlying reaction mechanisms [1–3]. Transfer reactions are also a competitive tool, beside studies of multiparticle correlations and nuclear structure, for production of neutron-rich unstable nuclei whose production is difficult by other methods. With the availability of radioactive beams, the transfer processes give access to a wide field of nuclear structure studies in the far-off-stability region. For example, production of superheavy elements [4–9] and neutron-rich nuclei in the $A \approx 200$ mass region [4,10–12] using multinucleon transfer reactions has been discussed. The multinucleon transfer processes may also play a crucial role in the synthesis of heavy elements with neutron-rich projectiles [13]. In view of its importance, a large amount of work on heavy-ion transfer reactions has been carried out in the past and is reported in the literature. Nice reviews on this subject can be found in Refs. [14,15], and references therein.

Though one- and two-nucleon transfer reactions have been studied extensively, reaction mechanisms involving transfer of many nucleons are not so well understood. The cross section for multinucleon transfer reactions depends on the projectile-target combination, and in general the cross section is rather small for projectile energies below the Coulomb barrier. With increasing bombarding energy the cross section usually increases and multiple transfers of nucleons become possible with significant cross section. However, at high incident energies, understanding the underlying transfer mechanism becomes complicated. The optimum Q value, "Q-opt" (Ref. [16]), shifts to higher negative value, thereby preferentially populating higher excited states in the final nuclei which are difficult to resolve experimentally due to the limited energy resolution. As a consequence, one deals with transfer cross sections which are result of integrations over a wide Q-value window, and a detailed understanding of the reaction mechanism aspect for such excitation-energy integrated data becomes complex. A systematic investigation of multinucleon transfer reactions and more experimental data using different target and projectile combinations would be needed for a better understanding of the reaction mechanism aspects.

The theoretical models such as GRAZING [17–19] and complex WKB (CWKB) [20], which are based on a direct reaction picture, have been used extensively in describing the distributions of mass, charge, and energy of outgoing fragments in different transfer channels [14,21–30]. In these models, multinucleon transfer processes are treated statistically using single-nucleon transfer probabilities calculated by first-order perturbation theory. These models are very

———————
[*]bjroy@barc.gov.in, bidyutr2003@gmail.com
[†]sekizawa@if.pw.edu.pl, kazuyuki.sekizawa@live.jp

successful for quantitative estimates of various observables
for multinucleon transfers between two heavy systems and at
bombarding energies below and around the Coulomb barrier.
However, the assumptions used in these semiclassical codes
are not well tested and may not be very suitable for reactions
involving light systems (eg., carbon, oxygen, etc.) at energies
much above the Coulomb barrier (as in the present case).

One of the important aspects of multinucleon transfer study
is to gain information on the multinucleon correlations in
nuclei, e.g., nucleon-nucleon pairing interactions that enhance
the transfer of pairs of nucleons in a collision between two
heavy ions. The fully microscopic time-dependent Hartree-
Fock (TDHF) calculation (Refs. [31,32], and references
therein) which is based on an independent particle picture
can be performed, though it is cumbersome, to compare
with measurement. The predictions from TDHF calculations
and a detailed comparison with experimental data, since the
theory does not include nucleon-nucleon correlations and any
clustering effects, can be attributed to the importance of such
correlations.

With a motivation to understand the heavy ion induced
multinucleon transfer reaction mechanism, we have studied
multinucleon transfer reactions in the system ^{18}O $+$ ^{206}Pb at
an incident energy above the Coulomb barrier. The reaction
^{16}O $+$ ^{208}Pb is well studied and is a benchmark in nuclear
reaction studies, as both the projectile and target are doubly
magic nuclei. However, the system ^{18}O $+$ ^{206}Pb has advantage
over ^{16}O $+$ ^{208}Pb for probing two-neutron correlations, as
the former has positive Q value for the two-neutron transfer
channel while no transfer channel with $Q > 0$ found in the
second system. Thus the cross section for the $2n$-transfer
reaction is expected to be large for this system.

In the present article we report the measurements of the
elastic scattering and multinucleon transfer angular distri-
butions carried out at an incident energy $\sim$1.6 times the
Coulomb barrier. The data are analyzed in the TDHF model,
and attempts have been made to include the effect of particle
evaporation. The measurement details are given in Sec. II
while experimental results are presented in Sec. III. The TDHF
calculation details and analysis of data are described in Sec. IV.
Section V presents a summary and conclusions of the present
work.

II. EXPERIMENTAL DETAILS

Experiments were performed with ^{18}O ions of energy
$E_{\text{lab}} = 139$ MeV obtained from the Pelletron-LINAC acceler-
ator, Mumbai. The energy uncertainty of the LINAC beam was
± 0.5 MeV. The target used was isotopically enriched ^{206}Pb
($>99\%$) of thickness 250 μg/cm^2 evaporated on ^{12}C foil (30
μg/cm^2). Reaction products were detected using three silicon
surface barrier (SSB) detector telescopes in ΔE-E configu-
ration mounted on two movable arms inside the 1.5 diameter
General Purpose Scattering Chamber at the LINAC beam hall.
The typical thickness of the ΔE detectors was $\sim$40 μm while
E detectors were about 1 mm thick. Two monitor detectors,
each consisting of a single SSB of thickness 1 mm, were
fixed at the forward angle $\theta_{\text{lab}} = \pm 20°$ with respect to the
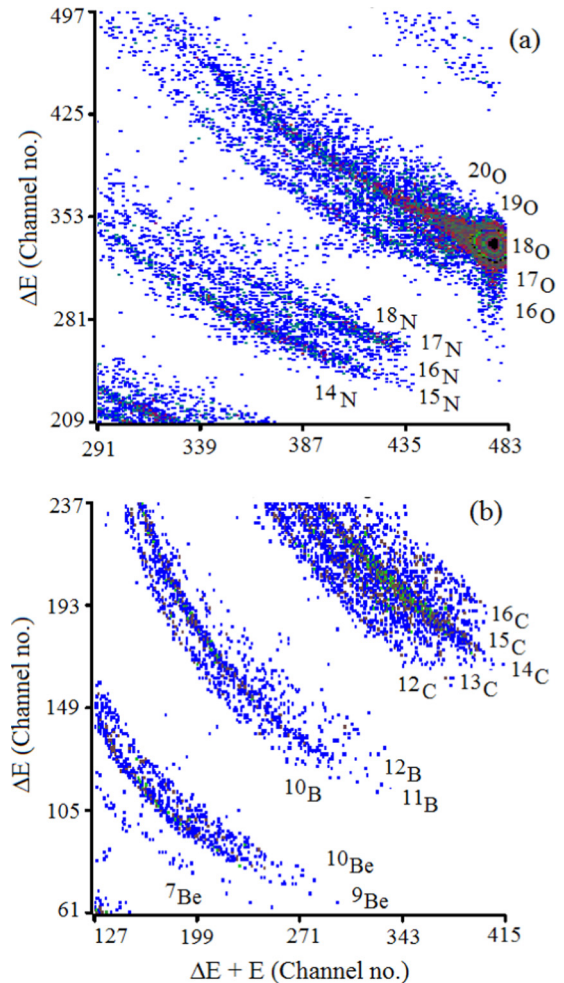beam direction and at 75 cm from the target for absolute

FIG. 1. (Color online) Typical two-dimensional ΔE-E spectra
from ^{206}Pb(^{18}O, x) reactions for the angle $\theta_{\text{lab}} = 30°$: (a) oxygen
and nitrogen isotopes and (b) carbon, boron and beryllium isotopes.

normalization of cross sections and relative normalization
between different runs. The relative solid angles between
the telescopes were measured by taking data at overlapping
angles. The angular resolution of the telescopes was less than
1.5°. The standard Versa Module Europa (VME) electronics
and computer acquisition system LAMPS (Linux Advanced
Multi-Parameter System) were used and the data were stored
as two-dimensional ΔE-E spectra. Typical ΔE-E spectra of
the light reaction products are presented in Fig. 1. As can be
seen, individual elements as well as isotopes are well resolved.
The particle identification (PI) spectrum was constructed from
the measured ΔE-E plot using the familiar algorithm

$$ PI = [(E + \Delta E)^b - E^b] = k \times M^{b-1} \times Z^2 $$

and the best result is obtained with $b = 1.75$. The calibration
curve for the isotope identification is shown in Fig. 2.

The Q value and angular distributions have been measured
for reaction channels involving transfer of up to nine nucleons.
The Q-integrated cross sections for various reaction channels
are obtained by appropriate selection of charge and mass
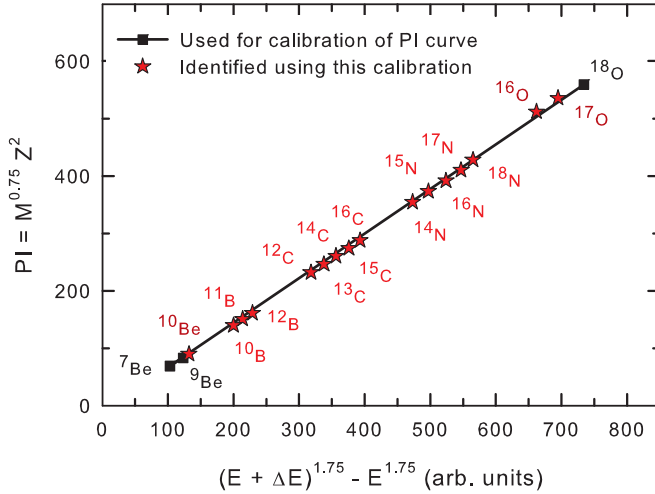of the reaction products. The cross sections, for a typical

FIG. 2. (Color online) Calibration curve showing mass identification of the projectile-like particles in ^{206}Pb(^{18}O, x) reactions. The elastically scattered ^{18}O particles and beryllium isotopes (^{7,9}Be) were used for calibration. The identification of ^{7}Be and ^{9}Be was straightforward as ^{8}Be, being unstable, is absent in the two-dimensional ΔE-E spectrum (Fig. 1).

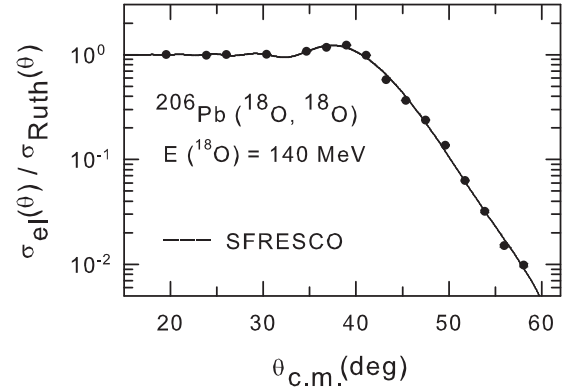

FIG. 3. Ratio of elastic scattering to Rutherford cross section for ^{18}O + ^{206}Pb at $E_{lab}(^{18}$O) = 140 MeV plotted as a function of the scattering angle. The fit shown is the optical model calculation using the code SFRESCO.

angle of $\theta_{lab} = 37°$, are listed in Table I along with the reaction Q values. Since Pb target contains ^{12}C backing, data were also collected with a pure carbon target for each of the angle measurements for background subtraction. The contribution from the ^{12}C target in the present angular distribution measurement is observed to be small. It is to be noted that the grazing angle for ^{18}O + ^{12}C at 139 MeV is about $\sim$10°.

III. RESULTS AND ANALYSIS

The measured elastic scattering angular distribution at 140 MeV is shown in Fig. 3. Data are plotted along with statistical errors, and in most of the cases the error bars are within the data symbol. The shape of the angular distribution is typical of Fresnel scattering, with an exponential fall beyond $\theta > \theta_{grazing} = 47°$. The differential cross sections are analyzed using the optical model (OM) search program SFRESCO [33] and the potential parameters have been derived. A volume Woods-Saxon form for the real and imaginary potentials is used. The OM potential parameters of ^{16}O + ^{208}Pb at an incident energy of 129.5 MeV (close to the energy of the present measurement) are used as starting parameters [34] for the analysis of the present ^{18}O + ^{206}Pb data. The values are also listed here in Table II. The same potential gives a good description of the ^{18}O + ^{206}Pb elastic scattering as well (the fitting procedure yields only about 1% change in the

TABLE I. Measured differential cross sections for various reaction channels in ^{18}O + ^{206}Pb for $E_{lab}(^{18}$O) = 139 MeV and θ_{lab} = 37°. Differential cross sections listed here are for the excitation-energy integrated data. The errors correspond to the statistical uncertainties. Reaction Q values (Q_o) listed in the table are ground state Q values.

Reaction	Q_o (MeV)	$d\sigma/d\Omega$ (mb/sr)
^{206}Pb(^{18}O, ^{20}O)	-3.25	5.2 ± 0.4
^{206}Pb(^{18}O, ^{19}O)	-4.13	50.6 ± 1.1
^{206}Pb(^{18}O, ^{17}O)	-1.31	45.4 ± 1.0
^{206}Pb(^{18}O, ^{16}O)	$+1.92$	21.2 ± 0.7
^{206}Pb(^{18}O, ^{18}N)	-17.65	2.5 ± 0.3
^{206}Pb(^{18}O, ^{17}N)	-12.38	19.6 ± 0.7
^{206}Pb(^{18}O, ^{16}N)	-11.38	6.2 ± 0.4
^{206}Pb(^{18}O, ^{15}N)	-6.41	22.0 ± 0.7
^{206}Pb(^{18}O, ^{14}N)	-12.64	1.8 ± 0.2
^{206}Pb(^{18}O, ^{16}C)	-20.79	3.2 ± 0.3
^{206}Pb(^{18}O, ^{15}C)	-18.08	3.6 ± 0.3
^{206}Pb(^{18}O, ^{14}C)	-11.64	24.1 ± 0.8
^{206}Pb(^{18}O, ^{13}C)	-15.26	9.1 ± 0.5
^{206}Pb(^{18}O, ^{12}C)	-14.20	6.8 ± 0.4
^{206}Pb(^{18}O, ^{12}B)	-29.31	1.8 ± 0.2
^{206}Pb(^{18}O, ^{11}B)	-26.66	1.2 ± 0.3
^{206}Pb(^{18}O, ^{10}B)	-33.24	0.9 ± 0.2
^{206}Pb(^{18}O, ^{10}Be)	-32.86	1.0 ± 0.2
^{206}Pb(^{18}O, ^{9}Be)	-34.75	1.3 ± 0.2

TABLE II. Potential parameters for ^{18}O + ^{206}Pb obtained from an optical model analysis of the measured elastic scattering cross sections using the computer program SFRESCO. The cumulative reaction cross section is also listed.

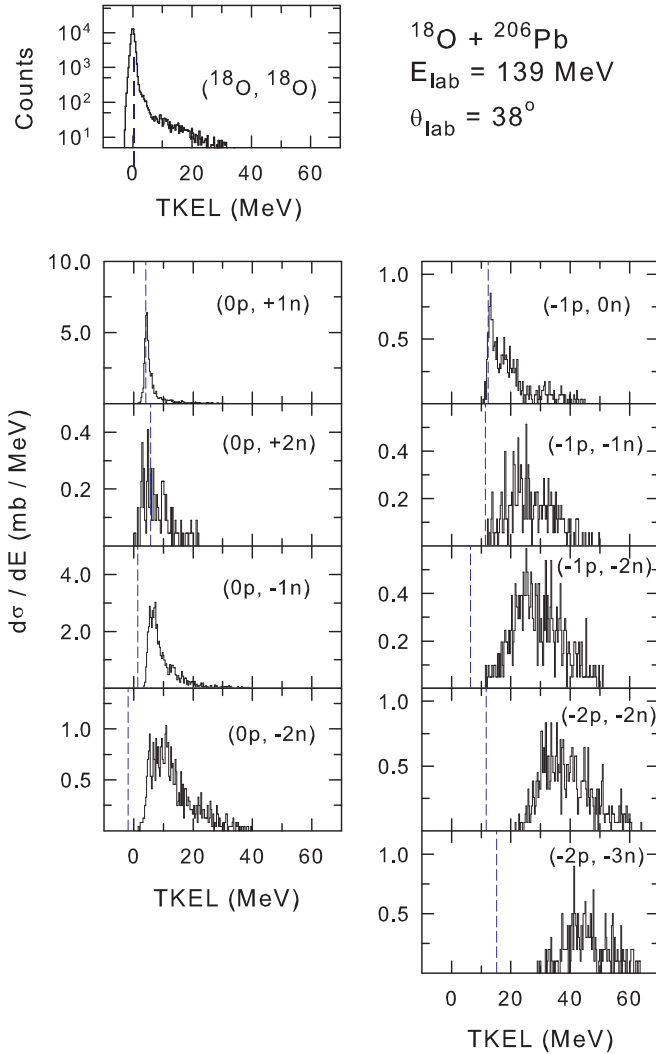| Potential parameters	^{16}O + ^{208}Pb at 129.5 MeV	^{18}O + ^{206}Pb at 140 MeV	^{16}O + ^{208}Pb at 138.65 MeV
V_o (MeV)	40.0	40.0	40.0
r_o (fm)	1.249	1.246	1.249
a_o (fm)	0.615	0.620	0.615
W (MeV)	35.0	35.0	35.0
r_i (fm)	1.249	1.244	1.249
a_i (fm)	0.615	0.609	0.615
Reaction cross section	2093 mb	2305 mb	2276 mb

FIG. 4. (Color online) Experimental total kinetic energy loss distribution (histogram plot) for quasielastic and various transfer processes in the $^{18}O + {}^{206}Pb$ reaction at $E(^{18}O) = 139$ MeV and $\theta_{lab} = 38°$. The vertical dashed lines (blue) indicate the position of ground-to-ground state Q values. The cross section scale (mb/MeV) has been obtained by normalizing each distribution to its total integrated cross section.

diffuseness parameters as shown in column 3 of Table II). The calculations also give almost same value of the reaction cross section (shown in the table) for these two systems when compared at the same center of mass energy of 128.75 MeV [corresponding to $E_{lab}(^{18}O) = 140$ MeV and $E_{lab}(^{16}O) = 138.65$ MeV]. The present study observes no significant changes in the OM potential and the reaction cross section in going from $^{16}O + {}^{208}Pb$ to $^{18}O + {}^{206}Pb$.

The experimental TKEL spectra (at $\theta_{lab} = 38°$) for the quasielastic, pure neutron stripping and pickup channels and some of the proton and neutron stripping reactions are shown in Fig. 4. The TKEL is constructed assuming binary reaction kinematics [35,36] and the experimental cross section scale (mb/MeV) has been obtained by normalizing each distribution to its total integrated cross section. It has been observed that for
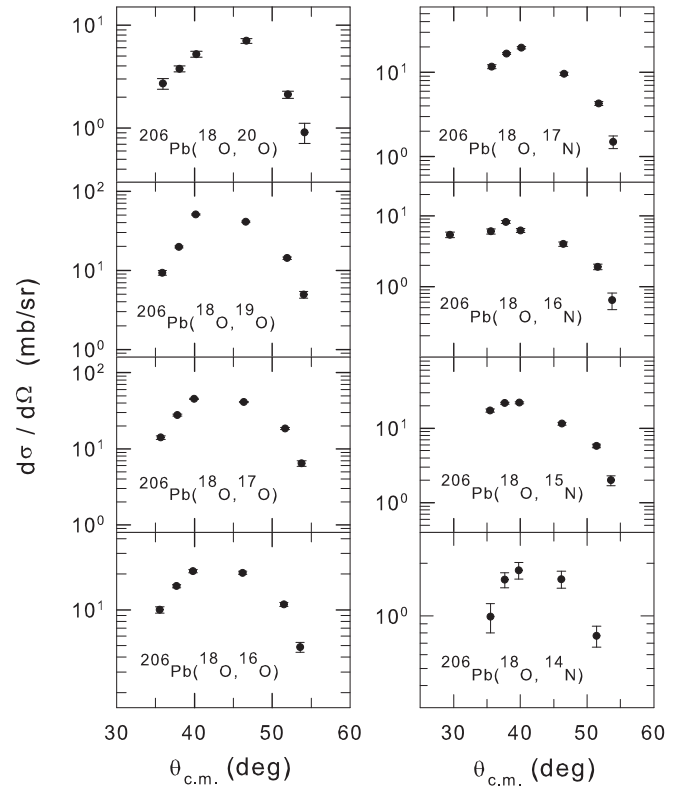

FIG. 5. Experimental Q-value integrated angular distributions for the indicated reactions at $E_{lab}(^{18}O) = 139$ MeV.

one-nucleon transfer reactions ($+1n$ and $-1p$ channels with some exceptions in the pure one-neutron stripping channel), the centroid of the TKEL spectra is close to the ground state Q value (as indicated by the dashed lines in the Fig. 4). There is a gradual shift of the centroid of energy loss spectra toward higher negative Q value as the number of nucleons transferred increases and the ground state population accounts for only a minor fraction of the total Q-integrated cross section. The present observation is similar to that found in other experiments (for example the work reported in Refs. [2,21]).

Angular distributions for Q-integrated cross sections for some representative channels are shown in Fig. 5. The angular distributions in general are bell shaped, indicating the grazing character of the reaction, peaking at an angle near the grazing angle (slightly below the grazing angle) with a small dependence on the channel. The average angular width is $\Delta\theta_{c.m.} \approx 15°$. Angular distributions become more forward-peaked with increasing number of nucleons transferred, and average widths also increase ($\Delta\theta_{c.m.} \approx 23°$). Total cross sections for different transfer processes have been obtained by integrating the angular distributions via a Gaussian fit. The fitting procedure introduces an error of 10–15 % in the final value of the cross section in most of the reaction channels except for ^{16}N, $^{13,12}C$, and $^{12,11}B$ where a somewhat higher value of error ($\sim$20–23 %) is obtained. The Q value and angle integrated cross sections for different reaction channels are shown in Fig. 6 as a function of the neutron number of the light ejectiles (each plot showing the isotope distribution for a particular proton stripping reaction).
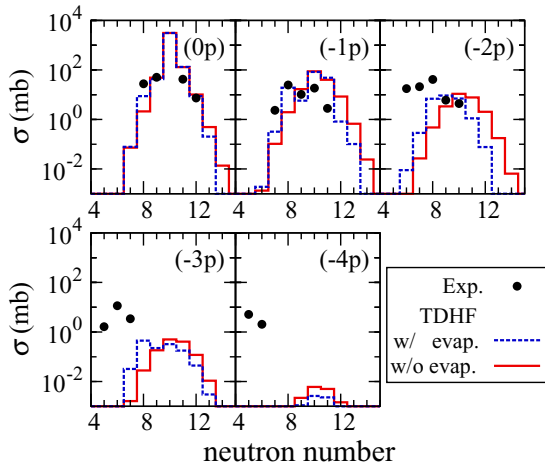
FIG. 6. (Color online) The total integrated cross section for various transfer channels in the ^{18}O + ^{206}Pb reaction at $E(^{18}$O) = 139 MeV. Points are the experimental data and the histograms represented by the red solid lines correspond to the results of present TDHF calculations. The predicted cross sections after inclusion of particle evaporation effects in the TDHF calculations are shown as blue dashed lines (details are given in the text).

In Fig. 7 we have replotted the total cross section data for stripping reactions as a function of the number of nucleons transferred ΔN. In general, the isotope production cross section for a particular element falls with the increase in number of transferred neutrons. For the $Z = 7$ element production cross section, it is observed that the cross section for ^{15}N, corresponding to three-nucleon ($1p2n$) stripping, is enhanced compared to the two-nucleon ($1p1n$) stripping (^{16}N production) and even compared to the one-proton stripping
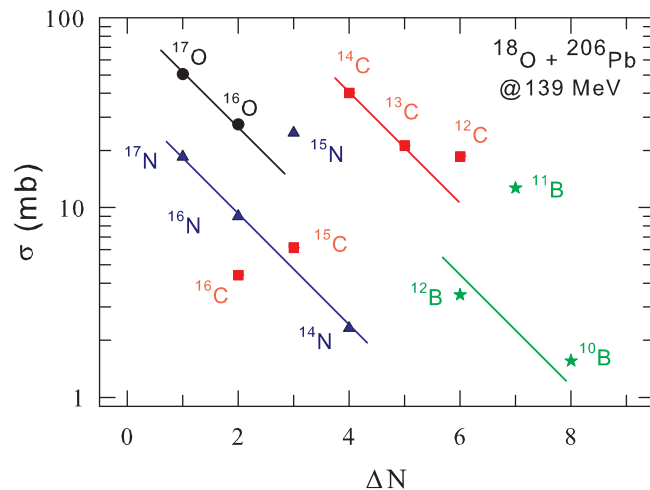

FIG. 7. (Color online) The Q-value and angle-integrated cross section for single- and multi-nucleon stripping reactions ^{206}Pb(^{18}O, x) measured at an incident ^{18}O energy of 139 MeV plotted as a function of the number of nucleons transferred ΔN. The solid lines are a guide for the eye and are drawn as a straight line to connect different isotopes of a particular element. All lines have the same slope.

(^{17}N production) cross section. In the carbon isotopes, the cross section for the four-nucleon ($2p2n$) transfer reaction is the highest and is expected as the α clustering in oxygen nuclei is well known. The cross section for the six-nucleon ($\alpha\,2n$) transfer process is observed to be relatively enhanced and is comparable to the (^{18}O, ^{13}C) reaction corresponding to five-nucleon ($\alpha\,n$) transfer. The present data are strongly indicative of $2n$-correlated transfer in some of the reaction channels that enhances the cross section for the corresponding isotope production. In our earlier study with ^{18}O projectile on ^{90}Zr target, the $2n$ transfer and $2n$-correlated transfer reactions are also observed to occur with a relatively large cross section [37].

The measured data are analyzed with a formalism developed in Ref. [32] using the TDHF calculation which, to our knowledge, is the only fully microscopic calculation for heavy ion multinucleon transfer reactions without nucleon-nucleon correlations. The formalism also allowed, to some extent, to include the effect of particle evaporation processes on the production cross section.

IV. TDHF CALCULATIONS AND COMPARISON WITH THE DATA

The present multinucleon transfer data are analyzed by employing a microscopic framework of the TDHF theory. The computational code of the TDHF theory for heavy ion reactions, developed by Sekizawa and Yabana [32], is used. Accuracy of the code was tested and it was successfully applied to describe multinucleon transfer processes in different systems. Because the theory is applicable to reactions at energies of $E \lesssim 10$ MeV/nucleon, the TDHF calculations are expected to be applicable to the present ^{18}O + ^{206}Pb reaction at $E(^{18}$O) $\simeq 7.7$ MeV/nucleon as well. The details of the formalism and its applications to other heavy ion transfer reactions are described in Ref. [32]. Here only a brief outline is given in connection to the present analysis.

In the code, a uniform spatial grid in three-dimensional Cartesian coordinates is used to represent single-particle wave functions without any symmetry restrictions. The ground state calculations are carried out with $30 \times 30 \times 30$ grid points, while for the reaction calculations grid points of $75 \times 65 \times 30$ have been used. The mesh spacing is set to be 0.8 fm, and for the derivatives the 11-point finite-difference formula is employed. We take the incident direction parallel to the negative x direction, and the impact parameter vector parallel to the positive y direction. The reaction plane is thus the xy plane. We set an initial separation distance between the projectile and target nuclei to be 24 fm parallel to the x axis.

For the energy density functional, we use a Skyrme-type functional with the SLy5 parameter set [38]. The ground state of ^{206}Pb is observed to have spherical shape while that of ^{18}O is of prolate shape with the deformation parameter $\beta \sim 0.19$. To examine orientation dependence of transfer dynamics, TDHF calculations are first performed for three different initial orientations of ^{18}O. The calculated average numbers of protons and neutrons in the projectile-like fragments (PLF) are plotted in Fig. 8 as a function of impact parameter. To calculate the average number of nucleons, the density
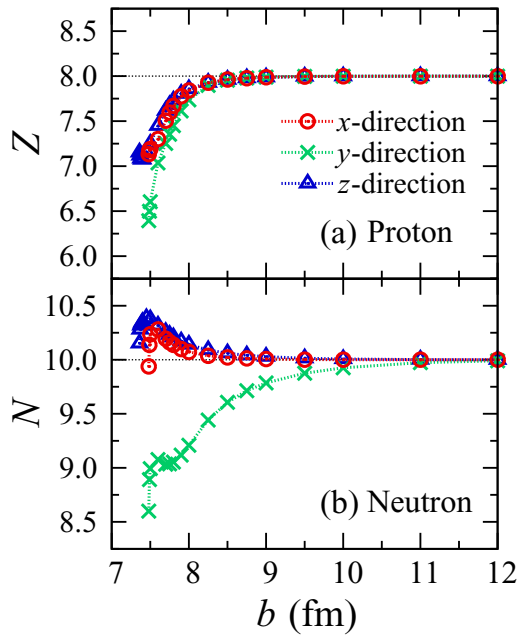
FIG. 8. (Color online) Average numbers of (a) protons and (b) neutrons in the PLF in ^{18}O + ^{206}Pb reaction at $E_{lab} = 139$ MeV plotted as a function of the impact parameter. Red open circles, green crosses, and blue open triangles connected with dotted lines show results for x-, y-, and z-direction configurations, respectively. The initial number of protons (neutrons) in ^{18}O is shown by a horizontal dotted line.

distribution is integrated over a sphere with radius of 13 fm around the center of mass of the PLF. As shown in the figure, the red open circles, green crosses, and blue open triangles connected with dotted lines are the results for x-, y-, and z-direction configurations, respectively. Each direction indicates a direction of the symmetry axis of ^{18}O in the initial TDHF wave function.

From the figure, a visible orientation dependence of transfer dynamics is observed. In low-energy heavy ion reactions, a fast charge equilibration process is usually observed, in which nucleons are transferred toward directions to reduce N/Z asymmetry between projectile and target nuclei. Because N/Z ratios of ^{18}O and ^{206}Pb are 1.25 and 1.51, respectively, we expect neutron transfer processes to take place from the nucleus ^{206}Pb to the nucleus ^{18}O and the proton transfer processes in the reverse direction. In the cases of x- and z-direction configurations, it has been observed that the nucleons are transferred toward the directions of charge equilibrium of the system. On the other hand, in the case of y-direction configuration, neutrons are transferred toward the opposite direction, which increases the N/Z asymmetry of the system. The difference may be related to properties of orbitals and matching of angular momentum between the projectile and target nuclei. The last occupied two-neutron orbitals in prolately deformed ^{18}O should be $K^{\pi} = 1/2^{+}$, which spatially extend along the symmetry axis. The last unoccupied two-neutron orbitals in ^{206}Pb are expected to be $3p_{1/2}$. This correspondence of angular momenta may originate the preference of neutron transfer from ^{18}O to ^{206}Pb

in the y-direction configuration. Although this orientation dependence of transfer dynamics contains interesting physics, it might not be possible to observe it in reality because the shape of the ^{18}O nucleus will be spherical because of the pairing correlation [39]. In the present work, we restrict ourselves to treatments ignoring any pairing effect and we show the results for calculations with the z-direction configuration only where the symmetry axis of ^{18}O is set perpendicular to the reaction plane, which shows ordinary transfer processes toward the charge equilibrium.

Using the position and momentum information of the outgoing nuclei in a TDHF wave function after collision, the scattering angle in the center-of-mass frame is evaluated. Several TDHF calculations with different impact parameters are then performed to obtain the deflection function, $\Theta(b)$. We extract transfer probability, $P_{tr}(b, N, Z)$, using the particle-number projection technique [32,40] from the TDHF wave function after collision. With these quantities in hand, the differential cross section for transfer reactions is then calculated by employing the relation

$$\frac{d\sigma(\Theta, N, Z)}{d\Omega} = \sum_i \frac{b_i}{\sin \Theta} \left| \frac{d\Theta(b_i)}{db} \right|^{-1} P_{tr}(b_i, N, Z), \quad (1)$$

where b_i ($i = 1, 2$) denotes an impact parameter at which the TDHF trajectory gives the same scattering angle [$\Theta = \Theta(b_1) = \Theta(b_2)$]. In order to find a correct set of b_i for a given scattering angle, a cubic-spline interpolation method is applied to the deflection function. The interpolation technique will also be used for evaluation of TKEL distributions as described later.

In Fig. 9, the differential cross sections evaluated by Eq. (1) are shown by solid curves in comparison with the measured cross sections for the one- and two-nucleon transfer reactions. The Coulomb rainbow angle, $\Theta_R \sim 45°$, is indicated by a vertical line above which TDHF has no trajectory. It is worth mentioning that the differential cross section as defined in Eq. (1) diverges, by definition, at the Coulomb rainbow angle. The calculated Coulomb rainbow angle, as can be seen from the figure, coincides with the peak position of experimental angular distributions. The TDHF angular distributions, though limited to the bright region ($\Theta_{c.m.} < \Theta_R$), give a reasonably good agreement with experimental data in some of the transfer channels that have relatively large cross section, e.g., (^{18}O, ^{19}O), (^{18}O, ^{17}O), (^{18}O, ^{17}N), (^{18}O, ^{20}O), and (^{18}O, ^{16}N). However, for the 2n-stripping reaction (^{18}O, ^{16}O), theoretical predictions underestimate the measurement significantly. Discrepancies have also been observed in some of the other reaction channels, and the discrepancy increases as the number of nucleons transferred increases.

Next, the transfer cross section $\sigma_{tr}(N, Z)$ is calculated by integrating the transfer probability over the impact parameter for the reaction channels where the PLF is composed of (N, Z) nucleons,

$$\sigma_{tr}(N, Z) = 2\pi \int_{b_{min}}^{\infty} b \, P_{tr}(b, N, Z) \, db. \quad (2)$$

The integration is evaluated numerically. The minimum of the integration is taken as 7.36 fm (the smallest impact parameter at which the binary fragments were observed) while the
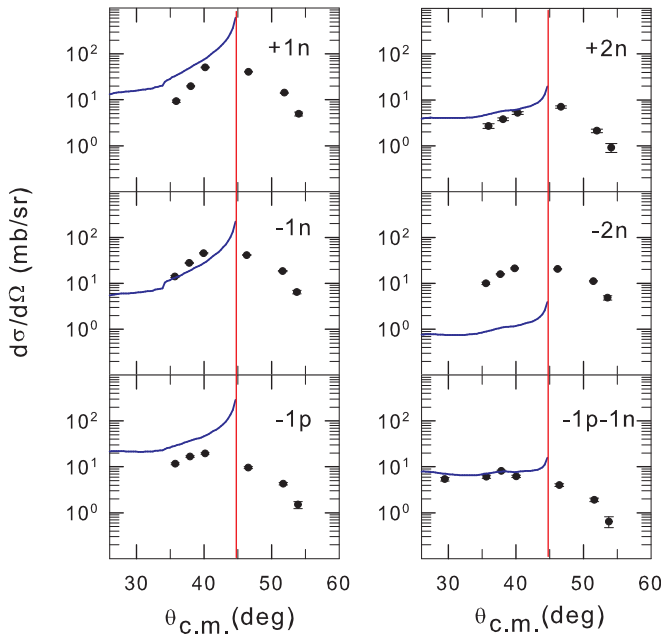
FIG. 9. (Color online) Differential cross sections of representative transfer channels as a function of the scattering angle for the ^{18}O + ^{206}Pb reaction at $E_{lab} = 139$ MeV compared with the TDHF calculations. The blue curves are the TDHF results and the red vertical lines indicate the position of the Coulomb rainbow angle obtained from the TDHF trajectories.

maximum is set to be 12 fm. The results for the integrated cross section for various transfer reaction channels, classified according to the number of transferred protons indicated by $(-x\mathrm{p})$, are plotted in Fig. 6 as a function of neutron number of the PLF. The points denote the measured cross sections while the histograms represented by red solid line are the results of the TDHF calculations without considering particle evaporation effects. As can be seen from the figure, for smaller numbers of nucleons transferred, e.g., $(0p-1n)$, $(0p+1n)$, $(0p+2n)$, $(-1p\,0n)$, $(-1p-1n)$, $(-2p\,0n)$, and $(-2p-1n)$, the agreement between theoretical predictions and measurements is reasonably good. As the number of nucleons transferred increases, the TDHF calculations fail to reproduce the experimental cross sections (calculated cross sections are smaller than the measured ones). Similar observations have also been noticed in an earlier study of multinucleon transfer reactions between different systems [32].

One of the possible reasons of disagreement between the theory and measurement might be the possible effect of particle evaporation and insufficient description of such processes in the TDHF calculations. In the calculations, the transfer probabilities and cross sections are calculated from a TDHF wave function typically at a time scale of $\sim 10^{-21}$ s, i.e., immediately after the two fragments were separated. Because the secondary processes like particle evaporation occur over a much longer time scale, the present calculations do not include such processes. We have made an attempt to include the effect of particle evaporation by evaluating evaporation probabilities using a statistical model and by extending the particle number projection technique, as detailed below.

In the following, we make an attempt to evaluate the effects of particle evaporation processes on transfer cross sections. Since such processes may not be described adequately in the present TDHF formalism, we have followed an approach as detailed in Ref. [41]. The expression for cross section [Eq. (2)] was simply extended by including the probabilities of particle evaporation. The evaporation probabilities are calculated by a statistical model [42] with the excitation energy of the outgoing fragments from which nucleons are evaporated as an input. The excitation energy, needed to estimate the number of nucleons to be evaporated, is calculated by applying the particle-number projection technique. The details are described in Refs. [41,43].

At first, we examined which are the transfer channels that will be more affected by the particle evaporation. To do this, the integrated cross section, $\sigma_{tr}(N,Z)$, was decomposed with respect to the TKEL as follows:

$$\sigma_{tr}(N,Z) = \int \frac{d\sigma(E,N,Z)}{dE}\,dE$$

$$\approx \sum_i \sigma_i(N,Z)\,\Delta E_i, \tag{3}$$

where $\Delta E_i \equiv |\mathrm{TKEL}_{i+1} - \mathrm{TKEL}_i|$ and $\mathrm{TKEL}_i \equiv \mathrm{TKEL}(b_i)$ denotes the TKEL evaluated from the TDHF wave function after the collision as described in Ref. [32]. $\sigma_i(N,Z) = \sigma(\mathrm{TKEL}_i,N,Z)$ is defined by

$$\sigma_i(N,Z) \equiv \frac{2\pi b_i P_{tr}(\mathrm{TKEL}_i,N,Z)\Delta b_i}{\Delta E_i}, \tag{4}$$

where $\Delta b_i \equiv |b_{i+1} - b_i|$. The calculated energy loss distributions for various transfer reactions, as evaluated using Eq. (4), are shown in Fig. 10. For the one-nucleon transfer channels, the cross section is observed to peak at low TKEL. For the two-neutron transfer reactions, the peak shifts slightly toward the higher TKEL and the spectrum has a long tail extending up to about 50 MeV. With more nucleons transferred, the peak of the TKEL distribution shifts toward a higher value and is about 40 MeV for five-nucleon transfer. For these reaction channels involving large kinetic energy loss, the PLFs can be at high excitation energy and are expected to evaporate more nucleons. A significant effect of particle evaporation on these transfer channels, contributed mainly from the large TKEL trajectories, is expected. The results of the present calculations, though performed for the angle integrated cross section, can be compared with the experimental TKEL plot in Fig. 4 and the general features of these spectra are about the same.

The calculations of the integrated cross section (angle and Q-value integrated) for each transfer channel including the evaporation processes have been performed. The results are shown in Fig. 6 by histograms (blue dashed line). As can be seen from the figure, the inclusion of effects of particle evaporation makes some improvement between the calculations and experimental data in some of the reaction channels. However, there remain large discrepancies in many of the transfer channels especially in the $2p$-, $3p$-, and $4p$-stripping reactions and the PLFs having neutron number less than 8.
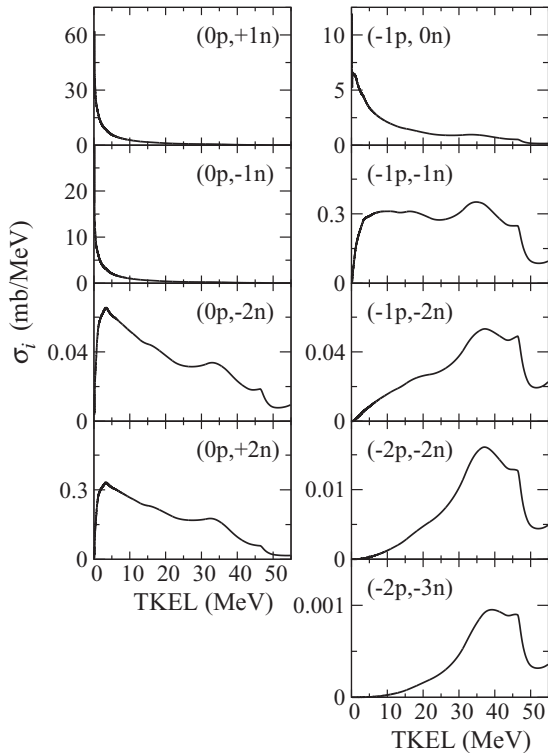
FIG. 10. The decomposed transfer cross sections as defined in Eq. (4) for various transfer reaction channels plotted as a function of TKEL (details are given in the text).

V. SUMMARY AND CONCLUSIONS

Cross sections for one-, two- and multinucleon transfer reactions in ^{206}Pb(^{18}O, x); $x = {}^{20,19,17,16}$O, ^{18,17,16,15,14}N, ^{16,15,14,13,12}C, ^{12,11,10}B, and ^{10,9}Be, have been measured at an incident ^{18}O energy of 139 MeV. A clear charge and isotope separation for projectile-like fragments has been achieved using silicon surface barrier detectors in a ΔE-E configuration. Transfer of up to nine nucleons has been observed. The differential and total cross sections and total kinetic energy loss distributions have been measured for the multinucleon transfer reactions. Strong enhancements were observed in the two-neutron correlated multinucleon transfer cross sections. The elastic scattering angular distribution has also been measured and an optical model analysis was performed. The present analysis, when compared with ^{16}O + ^{208}Pb at the same center-of-mass energy, indicates no significant changes in the OM potential and the reaction cross section between these two systems. Similar observations were also noticed in our earlier study [37] of the systems ^{18}O + ^{90}Zr and ^{16}O + ^{90}Zr. It was observed that the effect of two extra neutrons in ^{18}O is not significant on the elastic-scattering angular distribution and on the optical potential though the reaction cross sections for 2n and 2n-correlated transfer channels were seen to be enhanced compared to the ^{16}O + ^{90}Zr case.

Data are analyzed in a fully microscopic framework of the time-dependent Hartree-Fock theory. TDHF calculations give a reasonably good agreement with the measurement for transfer of a few nucleons; however, the theory becomes less

accurate as the number of nucleons transferred increases. Effects of particle evaporation on the cross sections are investigated by employing a statistical model. Inclusion of the evaporation effects gives some improvement towards the measurement; however, the calculations still underestimate the measured cross sections by a significant amount, especially for the cases where a large number of nucleons transferred are involved.

The discrepancies may partly originate from the mean-field nature of the TDHF theory. In the TDHF theory, nuclear dynamics is described from nucleons' degrees of freedom. The single-particle wave functions evolve under a *single* self-consistent mean-field potential that reflects average numbers of nucleons inside the potential. In reality, the potential is expected to be dependent on transfer channels. For example, when many protons are removed from ^{18}O, the potential felt by neutrons inside the PLF will be shallower, which may induce neutron transfer from projectile to target or suppress neutron transfer in the opposite direction. This kind of *correlation* which is caused by such a channel dependent potential is not sufficiently included in the TDHF description. The present experimental data might be indicative of the importance of inclusion of such channel dependent potentials in describing the multinucleon transfer processes. A promising way to improve the calculation is a use of the time-dependent generator coordinate method (TDGCM) [44,45]. Such TDGCM calculations, by including the channel-dependent mean-field potential and applying a density-independent energy density functional [46], may improve our understanding of the multinucleon transfer reaction mechanism. However, such calculations have not been performed in the present work.

It is also worth mentioning that the TDHF calculations are based on the independent particle picture; any correlation (pairing or clustering) in nuclei is not taken into account. The observed large disagreement between the TDHF calculations and present data might be indicative of the importance of nucleon-nucleon correlations in nuclei. Extending the present analysis by including the pairing correlation might provide satisfactory understanding of the multinucleon transfer processes. A time-dependent Hartree-Fock-Bogoliubov (TDHFB) theory [47–50] that treats the pairing correlation would provide a satisfactory description for such processes. However, such calculations for heavy ion transfer reactions, to our knowledge, are not yet available. Although a simplified method to include the pairing effects in the TDHF dynamics has been discussed in the literature [51–55], more realistic TDHFB calculations need to be developed.

[1] C. Y. Wu, W. von Oertzen, D. Cline, and M. W. Guidry, Annu. Rev. Nucl. Part. Sci **40**, 285 (1990).

[2] K. E. Rehm, Annu. Rev. Nucl. Part. Sci. **41**, 429 (1991).

[3] A. M. Stefanini, G. Nebbia, S. Lunardi, G. Montagnoli, and A. Vitturi, in *Proceedings of the International Workshop on Heavy-Ion Fusion: Exploring the Variety of Nuclear Properties*, 1994, Padova, Italy (World Scientific, Singapore, 1995).

[4] V. I. Zagrebaev and W. Greiner, Phys. Rev. C **83**, 044618 (2011).

[5] V. Zagrebaev and W. Greiner, J. Phys. G: Nucl. Part. Phys. **31**, 825 (2005).

[6] V. I. Zagrebaev, Yu. Ts. Oganessian, M. G. Itkis, and W. Greiner, Phys. Rev. C **73**, 031602(R) (2006).

[7] V. Zagrebaev and W. Greiner, J. Phys. G: Nucl. Part. Phys. **34**, 1 (2007).

[8] V. Zagrebaev and W. Greiner, J. Phys. G: Nucl. Part. Phys. **34**, 2265 (2007).

[9] C. Simenel, Eur. Phys. J. A **48**, 152 (2012).

[10] C. H. Dasso, G. Pollarolo, and A. Winther, Phys. Rev. Lett. **73**, 1907 (1994).

[11] C. H. Dasso, G. Pollarolo, and A. Winther, Phys. Rev. C **52**, 2264 (1995).

[12] V. Zagrebaev and W. Greiner, Phys. Rev. Lett. **101**, 122701 (2008).

[13] W. von Oertzen, in *Heavy Elements and Related Phenomena*, Vol. 1, edited by R. K. Gupta and W. Greiner (World Scientific, Singapore, 1999), p 68.

[14] L. Corradi, G. Pollarolo, and S. Szilner, J. Phys. G: Nucl. Part. Phys. **36**, 113101 (2009).

[15] W. von Oertzen and A. Vitturi, Rep. Prog. Phys. **64**, 1247 (2001).

[16] R. Bass, *Nuclear Reactions with Heavy Ions* (Springer-Verlag, Berlin, 1980).

[17] A. Winther, program GRAZING, http://www.to.infn.it/˜nanni/grazing.

[18] A. Winther, Nucl. Phys. A **572**, 191 (1994).

[19] A. Winther, Nucl. Phys. A **594**, 203 (1995).

[20] E. Vigezzi and A. Winther, Ann. Phys. (NY) **192**, 432 (1989).

[21] L. Corradi, J. H. He, D. Ackermann, A. M. Stefanini, A. Pisent, S. Beghini, G. Montagnoli, F. Scarlassara, G. F. Segato, G. Pollarolo, C. H. Dasso, and A. Winther, Phys. Rev. C **54**, 201 (1996).

[22] L. Corradi, A. M. Stefanini, D. Ackermann, S. Beghini, G. Montagnoli, C. Petrache, F. Scarlassara, C. H. Dasso, G. Pollarolo, and A. Winther, Phys. Rev. C **49**, R2875 (1994).

[23] L. Corradi, A. M. Stefanini, J. H. He, S. Beghini, G. Montagnoli, F. Scarlassara, G. F. Segato, G. Pollarolo, and C. H. Dasso, Phys. Rev. C **56**, 938 (1997).

[24] C. L. Jiang, K. E. Rehm, H. Esbensen, D. J. Blumenthal, B. Crowell, J. Gehring, B. Glagola, J. P. Schiffer, and A. H. Wuosmaa, Phys. Rev. C **57**, 2393 (1998).

[25] L. Corradi, A. M. Stefanini, C. J. Lin, S. Beghini, G. Montagnoli, F. Scarlassara, G. Pollarolo, and A. Winther, Phys. Rev. C **59**, 261 (1999).

[26] L. Corradi, A. M. Vinodkumar, A. M. Stefanini, D. Ackermann, M. Trotta, S. Beghini, G. Montagnoli, F. Scarlassara, G. Pollarolo, F. Cerutti, and A. Winther, Phys. Rev. C **63**, 021601(R) (2001).

[27] L. Corradi, A. M. Vinodkumar, A. M. Stefanini, E. Fioretto, G. Prete, S. Beghini, G. Montagnoli, F. Scarlassara, G. Pollarolo, F. Cerutti, and A. Winther, Phys. Rev. C **66**, 024606 (2002).

[28] S. Szilner, L. Corradi, F. Haas, G. Pollarolo, S. Beghini, B. R. Behera, E. Caurier, E. Fioretto, A. Gadea, A. Latina, G. Montagnoli, F. Nowacki, F. Scarlassara, A. M. Stefanini, M. Trotta, A. M. Vinodkumar, and Y. W. Wu, Eur. Phys. J. A **21**, 87 (2004).

[29] S. Szilner, L. Corradi, G. Pollarolo, S. Beghini, R. B. Behera, E. Fioretto, A. Gadea, F. Haas, A. Latina, G. Montagnoli, F. Scarlassara, A. M. Stefanini, M. Trotta, A. M. Vinodkumar, and Y. Wu, Phys. Rev. C **71**, 044610 (2005).

[30] S. Szilner *et al.*, Phys. Rev. C **76**, 024604 (2007).

[31] M. Evers, M. Dasgupta, D. J. Hinde, D. H. Luong, R. Rafiei, R. du Rietz, and C. Simenel, Phys. Rev. C **84**, 054614 (2011).

[32] K. Sekizawa and K. Yabana, Phys. Rev. C **88**, 014614 (2013).

[33] I. J. Thompson, Comput. Phys. Rep. **7**, 167 (1988); http://www.fresco.org.uk.

[34] J. B. Ball, C. B. Fulmer, E. E. Gross, M. L. Halbert, D. C. Hensley, C. A. Ludemann, M. J. Saltmarsh, and G. R. Satchler, Nucl. Phys. A **252**, 208 (1975).

[35] D. Montanari, L. Corradi, S. Szilner, G. Pollarolo, E. Fioretto, A. M. Stefanini, E. Farnea, C. Michelagnoli, G. Montagnoli, F. Scarlassara, C. A. Ur, S. Courtin, A. Goasduff, F. Haas, T. Mijatovic, and N. Soic, EPJ Web Conf. **63**, 02006 (2013).

[36] Y. H. Kim, Y. X. Watanabe, Y. Hirayama, N. Imai, H. Ishiyama, S. C. Jeong, H. Miyatake, S. Choi, J. Song, E. Clement, G. de France, A. Navin, M. Rejmund, C. Schmitt, G. Pollarolo, L. Corradi, E. Fioretto, D. Montanari, M. Niikura, D. Suzuki, H. Nishibata, and J. Takatsu, EPJ Web Conf. **66**, 03044 (2014).

[37] V. Jha, B. J. Roy, A. Chatterjee, and H. Machner, Eur. Phys. J. A **19**, 347 (2004).

[38] E. Chabanat, P. Bonche, P. Haensel, J. Meyer, and R. Schaeffer, Nucl. Phys. A **635**, 231 (1998); **643**, 441 (1998).

[39] S. Hilaire and M. Girod, Eur. Phys. J. A **33**, 237 (2007); http://www-phynu.cea.fr/science_en_ligne/carte_potentiels_microscopiques/carte_potentiel_nucleaire_eng.htm.

[40] C. Simenel, Phys. Rev. Lett. **105**, 192701 (2010).

[41] K. Sekizawa and K. Yabana, EPJ Web Conf. **86**, 00043 (2015).

[42] I. Dostrovsky, Z. Fraenkel, and G. Friedlander, Phys. Rev. **116**, 683 (1959); **119**, 2098 (1960).

[43] K. Sekizawa and K. Yabana, Phys. Rev. C **90**, 064614 (2014).

[44] J. F. Berger, M. Girod, and D. Gogny, Nucl. Phys. A **428**, 23 (1984).

[45] C. Simenel, J. Phys. G: Nucl. Part. Phys. **41**, 094007 (2014).

[46] J. Sadoudi, M. Bender, K. Bennaceur, D. Davesne, R. Jodon, and T. Duguet, Phys. Scr. **T154**, 014013 (2013).

[47] Y. Hashimoto and K. Nodeki, arXiv:0707.3083.

[48] B. Avez, C. Simenel, and Ph. Chomaz, Phys. Rev. C **78**, 044318 (2008).

[49] I. Stetcu, A. Bulgac, P. Magierski, and K. J. Roche, Phys. Rev. C **84**, 051309(R) (2011).

[50] Y. Hashimono, Eur. Phys. J. A **48**, 55 (2012).

[51] J. Blocki and H. Flocard, Nucl. Phys. A **273**, 45 (1976).

[52] S. Ebata, T. Nakatsukasa, T. Inakura, K. Yoshida, Y. Hashimoto, and K. Yabana, Phys. Rev. C **82**, 034306 (2010).

[53] G. Scamps, D. Lacroix, G. F. Bertsch, and K. Washiyama, Phys. Rev. C **85**, 034328 (2012).

[54] S. Ebata, J. Phys.: Conf. Ser. **454**, 012054 (2013).

[55] G. Scamps and D. Lacroix, Phys. Rev. C **87**, 014605 (2013).